33rd Annual International Conference of the IEEE EMBS
Boston, Massachusetts USA, August 30 - September 3, 2011

# Inertial Navigation System for Bladder Endoscopy

Alexander Behrens, Jonathan Grimm, Sebastian Gross, and Til Aach

***Abstract*— The usage of video endoscopes in cystoscopic interventions of the urinary bladder impedes an intuitive navigation. Although image–based solutions such as panorama images can provide extended views of the surgical field, a real–time 3–D navigation is not supported. Furthermore, the integration of common tracking systems in ambulant clinics is often hindered due to low usability and high costs. Thus, we discuss in this paper a first low–cost inertial navigation system. Our evaluation results show that in spite of lower sensor accuracies, mean errors between $< 1^\circ$ and $4^\circ$ are achieved for solid angles. Using endoscopes with different view angles we apply an extended endoscope model for an adaptive displacement correction. Furthermore, we implement a first guided navigation tool for tumor re–identification in real–time.**

## I. Introduction

The inspection of urinary bladder using video endoscopes is a standard intervention for diagnostics and therapy of bladder cancer. During this minimal invasive surgery (MIS) a small rigid endoscope is introduced into the bladder through the urethra to scan the internal bladder wall. Acquired by a camera, the endoscopic view is then displayed on a monitor. This indirect interaction impedes the surgeon's hand–eye coordination. Furthermore, the usage of endoscopes with angled optics, as well as the photo dynamic diagnostics (PDD), which show only a high fluorescent contrast for small distances between endoscope and bladder tissue $(d \leq 1cm)$, make a navigation more difficult. A successful and fast re–identification of tumors and lesions, observed e.g. in previous interventions may fail. Thus, a guided navigation tool is desired to lower the risk of missing tumors.

For computer–assisted bladder navigation several image mosaicking algorithms [1]–[3] are developed to provide cystoscopic panorama images, showing an extended field of view (FOV) of the bladder wall. Although these overview images can assist in orientation, documentation, and surgical planning, a direct 3–D navigation is not provided. Thus, external tracking devices are still required. Optical tracking systems would provide the best accuracy in positioning [4], but are less practical for cystoscopy, since they need a permanent line of sight between tracker and endoscope. Electromagnetic trackers may be more suitable, but their electromagnetic field can be disturbed by metallic materials nearby the operation field. Also the high acquisition costs impede an integration into ambulant clinics. The third major class of tracking devices represents low–cost inertial navigation systems (INS), which are not often considered for medical navigation assistance, since they show high systematic error due temporal drift effects. However, we discuss in this paper a first INS for cystoscopic interventions. Based on preliminary work [5], we evaluate its characteristics. Furthermore, we discuss an extended endoscope model adaptive to the view angle to increase the accuracy of the system, and developed a first guided navigation tool for tumor re–identification.

A. Behrens, J. Grimm, and T. Aach are with the Institute of Imaging & Computer Vision, Faculty of Electrical Engineering and Information Technology, RWTH Aachen University, Aachen 52062, Germany, (e-mail: behrens@lfb.rwth-aachen.de; aach@lfb.rwth-aachen.de)

## II. Inertial Navigation System

The developed navigation system consists of different micro–electro–mechanical systems (MEMS) like one accelerometer (ST LIS3L02AL) with three degrees of freedom and two gyroscopes (EPSON XV-3500CB). The sensors are orthogonally attached to the back end of the endoscope as shown in Fig. 1. Their values are read and analyzed with a

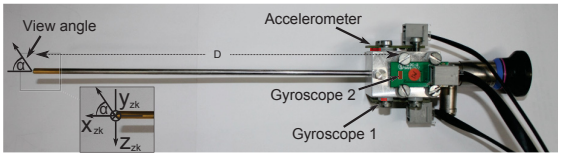


Fig. 1. Endoscope with view angle $\alpha$, and attached accelerometer and gyroscope sensors.

sampling rate of 300Hz for the gyroscopes, and 80Hz for the accelerometer, using a LEGO® Mindstorms® NXT Brick (32-Bit ARM Processor) and standard PC hardware.

In cystoscopic interventions the anatomy of the bladder reduces the degrees of freedom of the endoscope movement from six to four. The bladder opening forms with the urethra a fixed pivotal point. Thus, the endoscope movement is limited to a vertical- $R_\varphi$, horizontal- $R_\vartheta$, and axial rotation $R_\psi$, as well as a translation $r$ along the endoscope axis. Furthermore, authentic free–hand scans show only smooth endoscopic movements, which result in small tangential and centripetal accelerations compared to the gravitational acceleration. With these assumptions, the acceleration vector $\mathbf{a} = (a_x, a_y, a_z)^T$ is determined by the orientation of the sensor within the gravity field $(\mathbf{g} = g \cdot \mathbf{e_z})$ according to

$$\mathbf{a} \approx \mathbf{g_s} = R_\psi R_\varphi R_\vartheta \; \mathbf{g} = \begin{pmatrix} -\sin\varphi \; g \\ \sin\psi\cos\varphi \; g \\ \cos\psi\cos\varphi \; g \end{pmatrix}. \quad (1)$$

The solid angles $\psi$ and $\varphi$ are calculated by

$$\psi = \arctan\left(\frac{a_y}{a_z}\right), \quad \varphi = \arcsin\left(-\frac{a_x}{g}\right), \quad (2)$$

and the translation $r$ is derived from the integration

$$r = \left[ \iint (a_x - g_{s,x}) \; dt^2 \right]_0^T . \tag{3}$$

Since the accelerometer axis is aligned parallel to the direction of gravity, rotations $R_\vartheta$ around the z-axis cannot be measured. The solid angle $\vartheta$ is then calculated by using the gyroscopes. Assuming a constant value of $\psi$ during a short time interval $\Delta t$, $\vartheta$ is defined at time $T$ by

$$\vartheta(T) = \sum_{t=0}^{T} \int_{\tau=\Delta t} (\omega_{G_1}(\tau) \cos\psi_t + \omega_{G_2}(\tau) \sin\psi_t) \; d\tau, \tag{4}$$

with the angular velocities $\omega_{G_1}, \omega_{G_2}$ measured by the gyroscopes.

## III. Extended Endoscope Model

### A. Model Parameter

So far the position and orientation of an endoscope with a view angle of $\alpha = 0°$ (cf. Fig. 1) is calculated [5]. In this case the FOV is straight along the direction of the endoscope axis. A point $\mathbf{P}(\Phi = \varphi, \Theta = \vartheta)$ on the bladder surface is then projected into the image center of the endoscope camera, and its solid angles $\Phi, \Theta$ are determined directly by (2) and (4). In the case of using an angled endoscope ($\alpha \neq 0°$), the position of the observed point is not longer equal to the endoscope orientation ($\Phi \neq \varphi, \Theta \neq \vartheta$). Consequently, we extend our endoscope model to model also the direction of the view angle $\alpha$, as shown in Fig. 2. Point $\mathbf{P}(\Phi, \Theta)$ is then

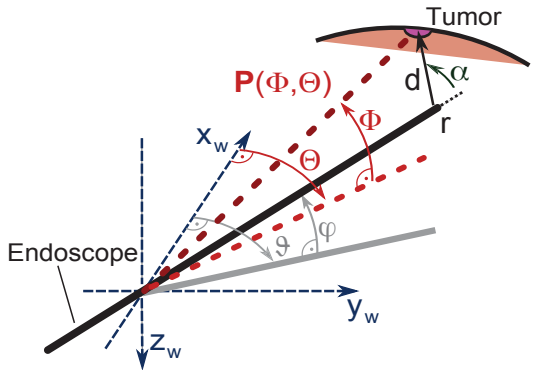


Fig. 2. Extended endoscope model, considering the viewing direction $\alpha \neq 0°$ to determine the position of a point $\mathbf{P}(\Phi, \Theta)$ on the bladder surface.

described by the position of the endoscope $(\varphi, \vartheta, \psi, r)$, its viewing direction $\alpha$, and its distance $d$ to the bladder wall. Using vector algebra, $\mathbf{P}(\Phi, \Theta)$ is determined by the sum

$$\mathbf{P} = \mathbf{r} + \mathbf{d} \tag{5}$$

(cf. Fig. 2), which leads to the equation system

$$\begin{aligned} \mathbf{A} &= \begin{bmatrix} \|\mathbf{P}(\Phi,\Theta)\| \cos\Phi \cos\Theta \\ \|\mathbf{P}(\Phi,\Theta)\| \cos\Phi \sin\Theta \\ \|\mathbf{P}(\Phi,\Theta)\| \sin\Phi \end{bmatrix} \\ &= \begin{bmatrix} r\cos\varphi\cos\vartheta \\ r\cos\varphi\sin\vartheta \\ r\sin\varphi \end{bmatrix} + \begin{bmatrix} d\cos(\varphi+\alpha_\varphi)\cos(\vartheta+\alpha_\vartheta) \\ d\cos(\varphi+\alpha_\varphi)\sin(\vartheta+\alpha_\vartheta) \\ d\sin(\varphi+\alpha_\varphi) \end{bmatrix}. \end{aligned} \tag{6}$$

The direction of $\mathbf{d}$ is given by the endoscope orientation $(\varphi, \vartheta)$ and the terms $\alpha_\varphi, \alpha_\vartheta$, which are both functions of $\alpha$ and $\psi$. To provide an analytical solution of (6), we model the bladder surface by a sphere. Given a radius $\varrho$, the surface points are then described by

$$\|\mathbf{P}(\Phi,\Theta)\| = 2\varrho \cos\Phi \cos\Theta. \tag{7}$$

In a first approximation the relations $\Phi \leftrightarrow \varphi$ and $\Theta \leftrightarrow \vartheta$ can be modelled by the sums

$$\Phi \approx \Delta\Phi + \varphi, \qquad \Theta \approx \Delta\Theta + \vartheta, \tag{8}$$

with the correction terms $\Delta\Phi, \Delta\Theta$.

Moving the endoscope into its zero position ($\varphi = \vartheta = 0$), we determine $\Delta\Phi$ and $\Delta\Theta$ using (6), (7) and (8). Finally, they become functions $f(\varrho, \alpha, \psi, r|d)$ dependent on the radius $\rho$ of the spherical bladder model, the view angle $\alpha$ of the applied endoscope, its axial rotation $\psi$, and its axial translation $r$ or the distance to the bladder wall $d$, respectively. Thus, the location of a tumor, which is seen in the center of the endoscope image can directly be determined by these parameters.

### B. View Angle Correction

After $\Delta\Phi$ and $\Delta\Theta$ are computed, they are used for view angle correction. For re–positioning, the target position of the endoscope and its rotation angles are determined in such a way that a given position $P(\Phi_{T_1}, \Theta_{T_1})$ of a specified region of interest (ROI) on the bladder surface, e.g. a tumor, is projected into the image center of the endoscope camera. Since the axial rotation can be chosen arbitrarily, we prefer an orthogonal view onto the surface described by

$$\psi_{T_1} = \arctan\left(\frac{\sin(\Theta_{T_1})}{\tan(\Phi_{T_1})}\right). \tag{9}$$

Given $\alpha$ and $\rho$, first the corrections terms $\Delta\Phi_{T_1}, \Delta\Theta_{T_1}$, and finally $\varphi_{T_1}, \vartheta_{T_1}$, and $r_{T_1}$ are calculated. They describe the resulting endoscope movement to reach the tumor position.

## IV. Results

For evaluation we use a hemispherical bladder phantom with 16 calibrated and color–coded markers, distributed across the surface, as shown in Fig. 3. To assess the accuracy of $\varphi$ and $\vartheta$ we move the endoscope eight times randomly from its zero position (pointing towards the center point on the phantom surface) to each reference marker by free–hand movements within a time period of $T \approx 5 \ldots 20s$. The trajectories of one reference point are illustrated in Fig. 4. The angle $\psi$ is evaluated in a second measurement, in which the endoscope is rotated freely around its axis while images are acquired simultaneously. By extracting the orientation notch in the images (cf. Fig. 4) using a template matching algorithm, reference values of $\psi$ are calculated. The resulting mean absolute errors (MAE) of the rotations and their standard deviations are listed in Table I. The calculation of the translation $r$ along the endoscope axis using (3) leads to unstable results, which keeps this parameter undetermined.

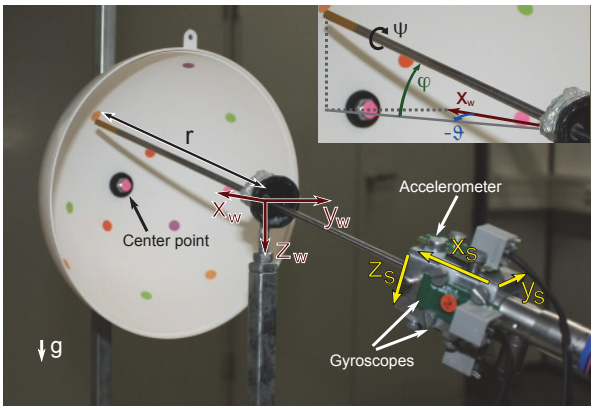


Fig. 3. Measurement setup showing a spherical bladder phantom with 16 calibrated markers, coordinate systems and rotation angles.

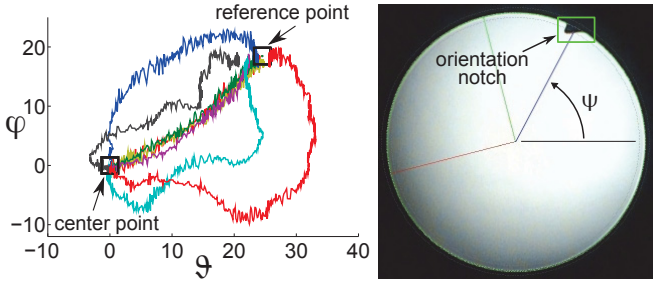


Fig. 4. Trajectories of free–hand movement of the endoscope from the center point to one reference marker of the bladder phantom (left). Calculation of $\psi$ based on the extraction of the orientation notch (right).

For evaluation of the extended endoscope model and the view correction, we use two endoscopes with different view angles ($\alpha = 12°, 70°$) in the measurement setup in Fig. 3. Again, the axis of each endoscope is first horizontally aligned with the center point of the phantom. Then the endoscope is guided eight times by a free–hand movement to each reference marker with an adequate and almost constant distance of $d \approx 3cm$, until the marker point is projected at correct scale into the center of the endoscope image. Since the direction of the FOV changes with axial rotations, the endoscope is freely rotated in $\psi$ to provide an almost orthogonal view to the surface. After the circular reference marker is detected in the image center by a real–time ellipse fitting algorithm, the end position is determined. Using (2) and (4) the angles $\psi, \varphi$, and $\vartheta$ are computed, whereas $\Phi$ and $\Theta$ are calculated by solving (6). The resulting MAE values are listed in Table II. For comparison of the remaining errors with and without view angle correction using the extended endoscope model, the MAE values of the vertical and horizontal rotations are plotted for both endoscopes in Fig. 5.

## V. Discussions

### A. Assessments

The evaluation results of the accelerometer from Table I show a small error of $\varepsilon_\varphi < 0.5°$ for the vertical rotations. This performance confirms the assumption that accelerations

| Movement | Parameter | MAE $\pm\ \sigma$ |
|---|---|---|
| Vertical Rotation | $\varphi$ | $0.39° \pm 0.28°$ |
| Horizontal Rotation | $\vartheta$ | $1.95° \pm 0.70°$ |
| Axial Rotation | $\psi$ | $3.37° \pm 2.44°$ |
| Translation | $r$ | – |

Mean absolute errors averaged over all reference points, for each endoscope motion parameter.

TABLE I

| Parameter | MAE $\pm\ \sigma$ 12° | 70° |
|---|---|---|
| $\varphi$ | $1.71° \pm 0.50°$ | $4.91° \pm 2.16°$ |
| $\Phi$ | $0.77° \pm 0.42°$ | $1.43° \pm 0.68°$ |
| $\vartheta$ | $2.10° \pm 1.22°$ | $5.70° \pm 2.52°$ |
| $\Theta$ | $1.99° \pm 1.02°$ | $2.23° \pm 1.39°$ |

Mean absolute errors averaged over all reference points with $(\Phi, \Theta)$ and without $(\varphi, \vartheta)$ view angle correction using the extended endoscope model.

TABLE II

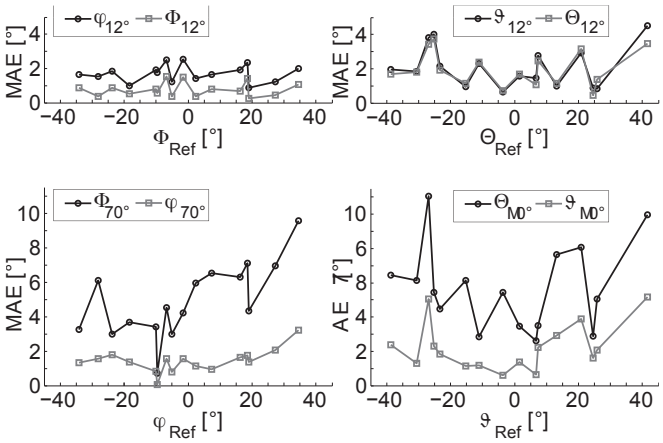


Fig. 5. MAE values of $\varphi, \Phi$ and $\vartheta, \Theta$ for the 12° (top row) and 70° endoscope (bottom row) at each marker position.

caused by a smooth endoscope movement can be neglected compared to gravity.

The MAE of the horizontal rotations shows an acceptable value of $\varepsilon_\vartheta \approx 2°$, although variations between $\varepsilon_\vartheta = 2° \ldots 7°$ may occur during single measurements due to temporal drift effects. Thus, too abrupt and very long endoscope movements would lead to less robust calculations of $\vartheta$. However, our results show that an endoscope movement in a time interval of $T = 5 \ldots 20s$, which is long enough to reach a specified tissue region for tumor re–identification, can be tracked sufficiently.

The axial rotations results in a higher error of $\varepsilon_\psi \approx 4°$. Although the calculated values are usually very close to the reference values, major deviations are assessed only during changes in axial directions, which then lead to a higher overall mean error. Given that the image–based orientation notch detection (cf. Fig. 4) shows a strong low–pass characteristic, the error values may be overrated. However, larger errors in $\psi$ will be irrelevant for small view angles endoscopes $\alpha \approx 0 \ldots 30°$, since the positions of their FOVs are less subjected to axial rotations.

The assessment of the view angle correction using the

extended endoscope model can be derived from the MAEs in Table II and the graph characteristics in Fig. 5. The results show that the applied correction terms reduce the positioning errors, describing the displacements between the projection of the reference points and the camera center, up to a factor of 2.5. In detail, the mean absolute errors for vertical and horizontal rotations are decreased each by a value of $\approx 3.5°$ to $\varepsilon_{\Phi,70°} = 1.43°$ and $\varepsilon_{\Theta,70°} = 2.23°$, compared to the basic endoscope model. In the case of a $12°$ endoscope, the errors in $\varphi$ are reduced to $\varepsilon_{\varphi,12°} = 0.77°$, whereas $\varepsilon_{\vartheta,12°} \approx 2°$ remains constant. Since $\Delta\Phi$ and $\Delta\Theta$ are functions of $\psi$, the error $\varepsilon_{\psi}$ remains equal to the values in Table I.

Fig. 5 shows equivalent results. As illustrated, the MAEs in horizontal and vertical direction of the $70°$ endoscope become significant lower for all reference points using the extended endoscope model. Again, the compensation effect drops with a smaller view angle of $\alpha = 12°$. However, the difference in $\varphi$ is about $\approx 1°$, whereas $\varepsilon_{\vartheta}$ remains constant.

Systematically, the correction terms $\Delta\Phi$ and $\Delta\Theta$ increase with a larger $\alpha$. From a geometrical point of view this may be explained by a larger view angle resulting in a FOV, which lies further away from the endoscope axis. This characteristic can also be verified mathematically by plotting their maximal values, as illustrated in Fig. 6. For $70°$ endoscopes maximal

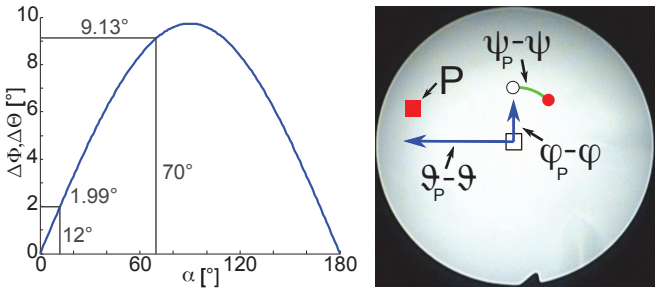


Fig. 6. Maximal values of $\Delta\Phi$ and $\Delta\Theta$ in dependency on the view angle $\alpha$, with $d = 3cm, \rho = 9cm, \psi = 0°$, and $\psi = 90°$, respectively (left). Navigation tool showing the angle differences between target and current endoscope positions (right).

correction terms of $\Delta\Phi = 9.13°$ and $\Delta\Theta$ can be applied, if $\psi = 0°$ and $\psi = 90°$, respectively. In the case of $\alpha = 12°$ the maximal compensation value is limited to $1.99°$. Thus, the low reduction of $\varepsilon_{\vartheta,12°}$ (cf. Table II) is justified, since the accuracy of $\vartheta$ lies in the same order of magnitude as the error correction.

### B. Navigation Tool

Based on these evaluation results we developed a guided navigation tool to re–identify specified ROIs, like tumors and lesions. Using the RealTimeFrame C++ framework [6], we implemented a real–time capable algorithm on a standard PC hardware (2.3GHz DualXeon Processor, 4GB RAM).

The overall workflow for navigation is as follows. First, the endoscope is moved to a specific anatomic landmark of the bladder, like the ureteral orifices, trigonum, or bladder ceiling. At this position the sensors are reset for calibration. With information about the view angle $\alpha$ of the endoscope, the relative position of the tumor location, and the desired view distance ($d \leq 1cm$) to the tissue, the target position of the endoscope is computed using view angle correction. The angle differences between target and current position are calculated, displayed in the endoscope image, and updated in real–time, as shown in Fig. 6. The current position is illustrated by a small blank rectangle in the image center, and the target point by a red one, respectively. The angle differences are visualized by two blue arrows, pointing into direction towards the target position. In the same way the difference $\psi_P - \psi$ is highlighted by a green arc between two virtual circles. The physician is then instructed to rotate the endoscope in vertical $(\Phi)$, horizontal $(\Theta)$, and axial $(\psi)$ directions to align the two rectangles and circles. Since the tracking of the current translation parameter $r$ is still undetermined, the endoscope is finally moved freely along its axis until the specific ROI, e.g. the tumor is visible in the FOV.

## VI. Conclusions

In this paper we developed and discussed a first low–cost inertial navigation system for cystoscopy. By tracking the endoscope motion with four degrees of freedom, its relative position is estimated from accelerometer and gyroscopes. To compensate the displacement between endoscope position and viewing direction determined by the view angle of the endoscope, we developed an extended endoscope model. Our evaluation results show that the mean position errors can then be reduced by a factor of 2.5 to an overall accuracy of $< 1.0°$, $\approx 2°$, $\approx 4°$ in vertical, horizontal and axial direction, respectively. Although the translation along the endoscope axis could not be computed reliably due to drift effects, we introduced nevertheless a first guided navigation tool for tumor re–identification in real–time. Based on these promising results clinical studies will be carried out in future work. Furthermore, inertial sensors with a higher resolution will be tested, and additional image–based information such as motion vectors will be analyzed.

## References


[1] A. Behrens, M. Bommes, T. Stehle, S. Gross, S. Leonhardt, and T. Aach, "Real-time image composition of bladder mosaics in fluorescence endoscopy," *Computer Science - Research and Development*, vol. 26, no. 1–2, pp. 51–64, 2011.

[2] A. Ben Hamadou, C. Soussen, W. Blondel, C. Daul, and D. Wolf, "Comparative study of image registration techniques for bladder video-endoscopy," in *Proc. SPIE Novel Optical Instrumentation for Biomedical Applications IV*, vol. 7371, 2009, pp. 737 118–1–7.

[3] R. Miranda-Luna, C. Daul, W. C. P. M. Blondel, Y. Hernandez-Mier, D. Wolf, and F. Guillemin, "Mosaicing of bladder endoscopic image sequences: Distortion calibration and registration algorithm," *IEEE Trans. on Bio. Engineering*, vol. 55, no. 2, pp. 541–553, 2008.

[4] W. Birkfellner, J. Hummel, E. Wilson, and K. Cleary, *Tracking Devices*, ser. Image-Guided Interventions. Springer, 2008, ch. 2, pp. 23–44.

[5] A. Behrens, J. Grimm, S. Gross, and T. Aach, "Trägheitsbasiertes Navigationssystem für die Harnblasenendoskopie," in *Bildverarbeitung für die Medizin 2011*, ser. Informatik aktuell. Springer, 2011, pp. 224–228.

[6] S. Gross, T. Stehle, A. Behrens, and T. Aach, "RealTimeFrame - a real time image processing solution for medical environments," in *41. DGBMT-Jahrestagung Biomedizinische Technik*. VDE, 2007.